Predicting the occurrence of rogue waves in the presence of opposing currents with a high-order spectral method

Guillaume Ducrozet [*]
Ecole Centrale Nantes, LHEEA Laboratory (ECN and CNRS), F-44321 Nantes, France

Maryam Abdolahpour
Faculty of Engineering and Mathematical Sciences, Oceans Graduate School, The University of Western Australia, Perth, Western Australia 6009, Australia

Filippo Nelli and Alessandro Toffoli [†]
Department of Infrastructure Engineering, The University of Melbourne, Melbourne, Victoria 3010, Australia

(Received 12 February 2021; accepted 27 May 2021; published 17 June 2021)

We discuss the dynamics of unidirectional random wave fields that propagate against an opposing current through laboratory experiments and direct numerical simulations of the Euler equations solved with a high-order spectral method. Both approaches demonstrate that the presence of a negative horizontal velocity gradient increases the probability of the occurrence of extreme and rogue waves in the course of their propagation with the emergence of a rapid transition from weakly to strongly non-Gaussian properties. Numerical simulations capture quantitatively well the statistical properties of laboratory observations and substantiate that underlying physics are associated to quasiresonant nonlinear interactions triggered by the background current.

DOI: 10.1103/PhysRevFluids.6.064803

I. INTRODUCTION

Rogue waves are exceptional events with a crest-to-trough height exceeding two times the significant wave height, namely, the average of the highest one-third of the waves in a 20-minute record [1]. Once believed to be a sailors' myth, several observations of rogue waves have been made in the open ocean [2–6]. These measurements have been demonstrated theoretically [7–9] and reconstructed in laboratories [10–16]. Rogue waves have also been responsible for a number of ship accidents worldwide [6,17–19].

Assuming the medium in which waves propagate is homogeneous in space and time (i.e., it exhibits unique features), there are several mechanisms than can cause rogue waves in the ocean: the linear superposition of Fourier modes, second-order nonlinear effects, crossing sea states, and shallow water effects, among others (see, e.g., [6,9,20–24]). The most acknowledged, however, is the instability of uniform wave packets to side band perturbations, i.e., a high-order nonlinear mechanism known as modulational instability (e.g., [10,25–30]). Provided that the waves are sufficiently steep (i.e., nonlinear) and the energy spectrum is centered around a dominant (peak) frequency and direction (i.e., the sea state is narrow banded and unidirectional), modulational instability prompts a transfer of energy across the dominant mode and side bands, which forces individual waves to grow within a short space on a scale of tens of wavelengths.

[*]guillaume.ducrozet@ec-nantes.fr
[†]toffoli.alessandro@gmail.com

Within a stochastic framework, high-order nonlinearity results in a heavy-tailed probability density function (PDF) of the wave displacements, which strongly deviates from a Gaussian distribution [10,25–28,31,32]. There is evidence, however, that realistic oceanic conditions are less prone to modulational instability due to commonly broad directional wave energy spectra. Therefore, the PDF only weakly deviates from Gaussian statistics and can be accurately predicted by second-order nonlinear theories [24,33,34]. It is worth noting, nevertheless, that this does not necessarily mean that higher-order nonlinear effects are idle in nature. There is experimental evidence in this respect showing that modulational instability is still responsible for nonlinear energy transfer and breaking dissipation in a more realistic directional sea state without necessarily leading to non-Gaussian statistics [35–37].

Interestingly, pronounced deviations from Gaussian statistics can hold in broad banded sea states if the medium has nonhomogeneous properties (e.g., [13]). Inhomogeneity can emerge because of time-varying wind forcing [38], a nonflat bottom profile [39–41], or the presence of varying current [13,42,43]. In this respect, a significant number of ship accidents due to bad weather and heavy sea conditions have been reported in regions of strong oceanic currents, such as the Gulf Stream, the Agulhas Current, and the Kuroshio Current, or tidal currents (e.g., [18,44,45]). It is not a mystery that rogue waves can develop as a result of the interaction with strong currents (notorious is the region of the Agulhas current that is east of South Africa [44]). One possible mechanism in these circumstances triggers when waves propagate with opposite or oblique direction to a surface current. Provided the current is fast enough, wave energy is forced to refract and coalesce in certain areas with a consequent formation of large waves as a result of a linear focusing (see caustic theory [45,46]).

According to the linear dispersion relation, an opposing current compresses the wave profiles due to a Doppler shift. This forces the wavelength to shrink and wave height to increase, with a consequent enhancement of the wave steepness and nonlinearity (e.g., [42,45]). Note that this transition can be further accelerated by concurrent refraction and directional focusing. A number of laboratory experiments have been undertaken to verify the nonlinear dynamics of regular and irregular waves when opposing a strong current (see, for example, [13,43,47–51], among others). Tests on regular (deterministic) waves have shown that the increase of wave steepness makes wave trains susceptible to modulational instability and thus more prone to rogue waves, even if wave conditions would be stable otherwise [49]. Rogue waves under these circumstances can be interpreted as a signature of out-of-equilibrium dynamics [39]. In irregular random wave fields, opposing currents induce a sharp and rapid transition from weakly to strongly non-Gaussian sea states [13,43]. Although changes of wave statistics are consistent with deterministic experiments and theory [49,52], experimental results only confirm that currents can locally increase steepness, force rogue waves to emerge, and lead to non-Gaussian statistics, but do not substantiate the controlling physics. Irregularities in experimental current fields can, in fact, refract waves, redirecting them towards the side walls, reflect them towards the center of the basin, and consistently force energy to focus somewhere in the basin [43,51], similarly to what caustic theory would predict [45,46]. Therefore, the occurrence of large amplitude waves in experimental facilities might be simply explained by a linear directional focusing rather than nonlinear interactions.

Here, we revisit an experimental model of wave-current interaction, which was conducted in a wave flume, i.e., free of directional effects [13]. Observations are reassessed by comparing them against numerical simulations from current-modified Euler equations, in order to underpin the physics driving the generation of rogue waves in the presence of an opposing current. The paper is organized as follows: Secs. II and III detail the experimental setup and the numerical model; Sec. IV describes the evolution of the wave field in terms of significant wave height and spectral density; Sec. V discusses statistical properties of the surface elevation and emergence of rogue waves; and Sec. VI provides concluding remarks.

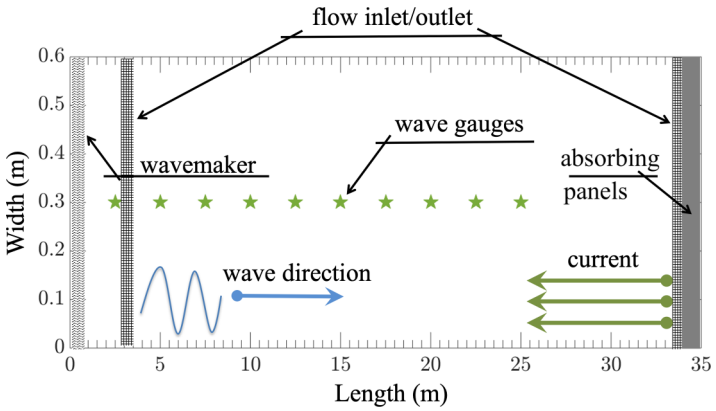

FIG. 1. Schematic representation of the wave-current experimental facilities (not to scale).

II. THE PHYSICAL MODEL

A. Facility and experimental setup

The experiments were conducted in the wave flume at the Coastal, Ocean And Sediment Transport (COAST) laboratory of the University of Plymouth. The facility is 35 m long, 0.6 m wide, and with a uniform water depth d of 0.75 m (see Fig. 1). The waves were generated by a piston wave maker with active force absorption at one end of the tank. Absorbing panels were installed at the other end of the tank to prevent wave reflection. The flume was also equipped with pumps for water circulation, which mimics a background current U up to 0.5 m/s. Water flow can follow or oppose the wave direction of propagation, but only an opposing current was used herein. Either the inlet or outlet was located near the absorbing panels, while the other was at a distance of 2.5 m from the wave maker. This particular configuration allows waves to be generated outside the current field and propagate for a few wavelengths before encountering a current gradient. For a complete discussion of these experimental tests, including directional wave fields generated in the ocean wave basin of the COAST Laboratory of Plymouth University, see [13,14].

The wave field was monitored with 10 capacitance wave gauges equally spaced (every 2.5 m) along the flume and located at its center in the transverse direction (see Fig. 1). Furthermore, the velocity field was measured with two properly seeded acoustic doppler velocimeters (ADVs). The instrumentation was operated at a sampling frequency of 128 Hz.

A survey of the current was conducted by measuring 10-min series at several distances from the wave maker and depths. Due to the particular configuration of the flume, there is no current close to the wave generation system, while a strong velocity gradient forms at $x = 2.5$ m in the proximity of the inlet or outlet. Stable water flow both longitudinally and transversely was observed starting at about 3 m from the wave maker [see the averaged profiles in Figs. 2(b) and 2(c)]. The vertical profile also reveals a uniform current flow until a depth of 0.4 m, below which a parabolic profiles emerges [Fig. 2(a)]. Over the entire time series, the standard deviation was approximately 10% (with peaks at high current speeds); temporal variations occurred within a period of approximately 10 s.

Unidirectional, irregular wave fields were generated by imposing a predefined motion at the wave maker. The piston displacements were computed by converting a target wave spectrum into a voltage, using an inverse fast Fourier transform method with random amplitudes and phases approximations and the linear transfer function to account for the wave maker geometry. For a selected sea state, experimental tests were conducted for a total period of 1 h. Two realizations with different random amplitudes and phases were carried out to ensure enough data for the statistical analysis.

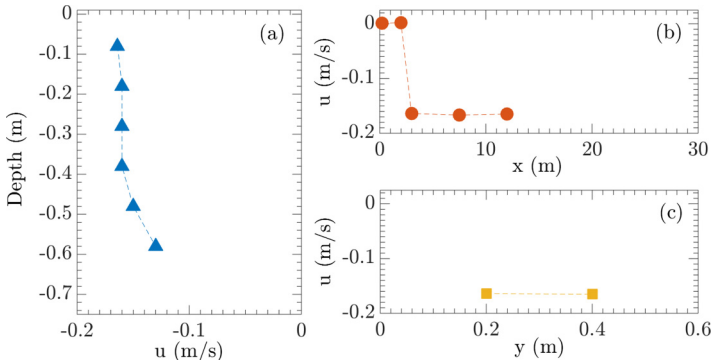

FIG. 2. (a) Vertical, (b) longitudinal, and (c) transverse profiles of the horizontal current velocity.

B. Initial conditions

Initial conditions for random wave fields were specified using a JONSWAP spectrum $E(f)$ [53], where f is the wave frequency. The spectral shape was defined by a peak period $T_p = 0.8$ s (wavelength $L_p = 1$ m, group velocity $C_g = 0.63$ m/s, and relative water depth $k_p d = 4.7$, where k_p is the wave number associated to the peak period), significant wave height $H_s = 4\sqrt{m_0} = 0.025$ m, where m_0 is the variance of the wave spectrum, and peak enhancement factor $\gamma = 3$. The resulting wave field was characterized by a wave steepness $k_p H_s/2 = 0.08$, which is a typical value for moderate sea states [18].

The evolution of the input wave field was measured with no current for the benchmark. Experiments were then repeated with opposing currents at nominal velocities of $U = -0.04, -0.06, -0.12, -0.18$, and -0.24 m/s, which corresponds to $U/C_g = -0.06, -0.10, -0.19, -0.29$, and -0.38. Although dominant wave components around the spectral peak are far from the blocking condition ($U/C_g = -0.5$ [1]), it is worth noting that high-frequency modes may be subjected to blockage due to slower group velocities.

III. A CURRENT-MODIFIED HIGH-ORDER SPECTRAL MODEL

The evolution of the wave field was simulated by numerically integrating the potential Euler equations with a high-order spectral (HOS) method, using the open-source solver HOS-OCEAN [54]. The numerical scheme is based on an efficient algorithm that computes a series expansion in the wave steepness of the vertical velocity, enabling the inclusion of an arbitrary degree of nonlinearity in the computation. A third-order expansion is used herein to model the modulational instability (see [55,56]). HOS has been extensively validated and used in various applications, such as the analysis of complex wave phenomena, including the emergence of rogue waves [28,57,58].

A current-modified version of HOS-OCEAN is applied to account for the background current (see details in [59,60]). The theoretical and numerical aspects of this modification are similar to the ones discussed in [13,14,52], in the context of the nonlinear Schrödinger equation. The current is idealized by assuming it to be slowly varying in both the vertical and the horizontal directions. This ensures the correctness of the potential flow formalism to model wave-current interactions [60]. To include a spatially varying current in the HOS-solver, the free-surface elevation $z = \eta(\mathbf{x}, t)$ is decomposed into a component due to the stationary current $\eta_c(\mathbf{x})$ and a counterpart associated to the waves $\eta_w(\mathbf{x}, t)$. The contribution of the current is defined by its horizontal velocity $\mathbf{u_c}$ at the mean water level $z = 0$, through the current-only free-surface boundary condition,

$$g\eta_c + \tfrac{1}{2}(\mathbf{u_c} \cdot \mathbf{u_c} + [\mathbf{u_c} \cdot \nabla \eta_c]^2) = 0, \tag{1}$$

where ∇ stands for the horizontal gradient.

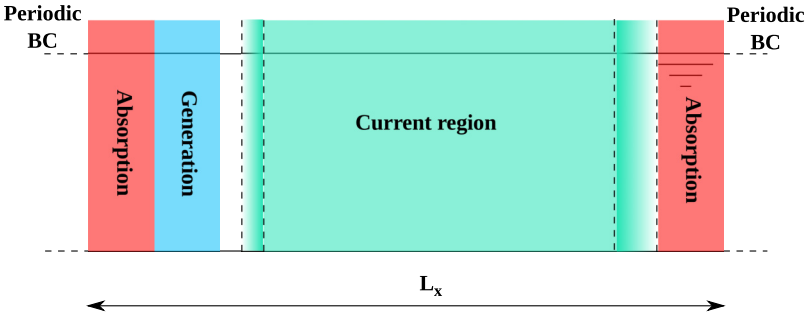

FIG. 3. Configuration of the numerical solution.

The wave counterpart $\eta_w(\mathbf{x}, t)$ is computed numerically assuming (i) the current is slowly varying in the vertical direction and (ii) the current is slowly varying in the horizontal direction, i.e., $|\nabla\eta_c| \ll |\nabla\eta_w|$. Based on these assumptions, a new set of free-surface boundary conditions is derived for $\eta_w(\mathbf{x}, t)$, considering $z = \eta_c(\mathbf{x})$ is the new reference level of vertical coordinates. Those boundary conditions are written on $z = \eta_w(\mathbf{x}, t)$ as follows:

$$\frac{\partial\eta_w}{\partial t} = (1+|\nabla\eta_w|^2)W_w - \nabla\phi_w^s\cdot\nabla\eta_w - \mathbf{u_c}\cdot\nabla\eta_w - \eta_w(\nabla\cdot\mathbf{u_c}) + (\mathbf{u_c}\cdot\nabla\mathbf{u_c})\nabla\phi_w^s - 2(\mathbf{u_c}\cdot\nabla\mathbf{u_c})\cdot\nabla\eta_w + (\mathbf{u_c}\cdot\nabla\mathbf{u_c})\cdot(\mathbf{u_c}\cdot\nabla\mathbf{u_c}), \tag{2}$$

$$\frac{\partial\phi_w^s}{\partial t} = -g\eta_w - \frac{1}{2}\left|\nabla\phi_w^s\right|^2 + \frac{1}{2}(1+|\nabla\eta|^2)W_w^2 - \mathbf{u_c}\cdot\nabla\phi_w^s - [(\mathbf{u_c}\cdot\nabla\mathbf{u_c})\cdot\nabla\eta_w]W_w^2 + \left[\frac{1}{2}(\mathbf{u_c}\cdot\nabla\mathbf{u_c})\cdot(\mathbf{u_c}\cdot\nabla\mathbf{u_c})\right]W_w^2 + \eta_w[-(\mathbf{u_c}\cdot\nabla\mathbf{u_c})\cdot\mathbf{u_c}](\nabla\cdot\mathbf{u_c}). \tag{3}$$

The system given by Eqs. (2) and (3) is solved with a standard HOS-solver, with ϕ_w^s standing for the free-surface velocity potential induced by waves and W_w the vertical velocity at the free surface. The total free-surface elevation is eventually reconstructed as a superposition: $\eta(\mathbf{x}, t) = \eta_c(\mathbf{x}) + \eta_w(\mathbf{x}, t)$.

A schematic representation of the numerical configuration is given in Fig. 3. In order to satisfy the periodicity of the numerical solution, we set up different relaxation zones, allowing the control of the wave field interacting with the current. The waves are generated on one side (the left-hand side in Fig. 3) and absorbed at the other side. The control of periodicity, generation and absorption have been validated in the context of the efficient modeling of wave-bottom interactions using a HOS-solver [61,62]. In the present configuration, this is associated with a spatially varying current.

The numerical model includes a classical de-aliasing procedure [63,64] to hamper contamination from an unnatural cascade of energy to very high-frequency modes. Two additional dissipation terms are implemented to account for: (i) side-wall friction and (ii) wave breaking dissipation. The former is based on theoretical predictions in [65]. The latter is included in HOS-solvers by a local modification of the free-surface boundary conditions given by Eqs. (2) and (3). A robust breaking-onset parameter is used to detect the time and location of breaking events [66], allowing the introduction of relevant diffusion terms in those boundary conditions [67].

A detailed convergence study has been carried out in order to choose the relevant spatial and temporal resolution. The computational domain is discretized with 4096 modes, free of aliasing errors, and the time tolerance of the adaptive Runge-Kutta scheme is fixed to 10^{-8}. The numerical simulations are 20 minutes long (around 1500 wave periods) and, for each configuration, 200 different realizations with random phases are computed in order to obtain highly accurate statistics of the extreme events.

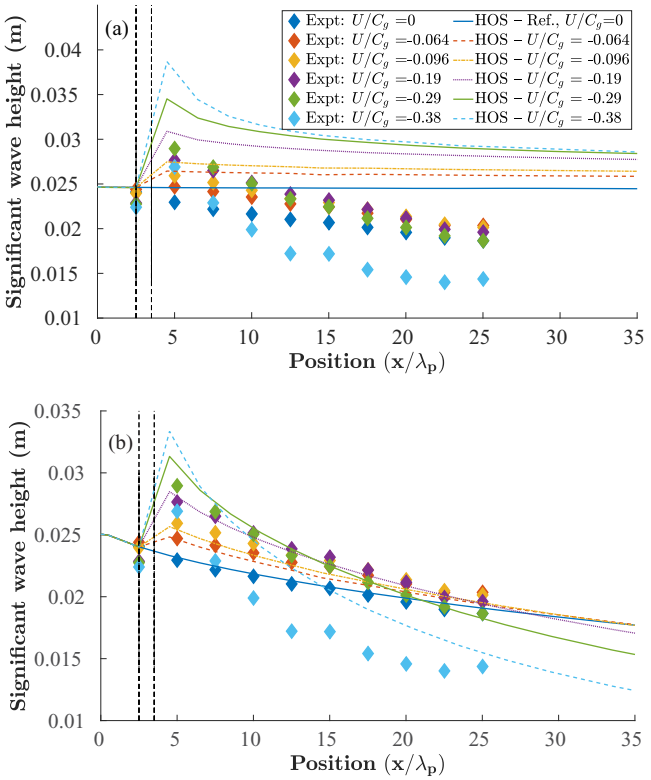

FIG. 4. Evolution of significant wave height H_s as a function of the nondimensional distance x/L_p from the wave maker for different current speeds: (a) without and (b) with wall friction dissipation. Marks indicate experimental observations, the solid lines refer to numerical simulations, and the dashed vertical lines indicate the start and end of the transition region from no current to regime flow.

IV. SIGNIFICANT WAVE HEIGHT AND SPECTRAL DENSITY

A. Significant wave height

Figure 4 presents the evolution of experimental and model significant wave height, H_s, as a function of the nondimensional distance from the wave maker (i.e., x/L_p, where x is the absolute distance from the wave maker) for different current speeds. To assess the dissipation along the flume, model runs with the wave breaking dissipation term only are shown in Fig. 4(a), while runs with the combined breaking and friction modules are presented in Fig. 4(b).

In the absence of a background current, experimental observations show an evident drop of H_s with distance from the wave maker (about 20% reduction after 25 wavelengths). The low steepness of the initial condition inhibits high-order nonlinearity and hence growth of individual waves, preventing the development of wave breaking within the flume (cf. [68]). As a result, the breaking dissipation term does not capture the observed decay [Fig. 4(a)], which is therefore attributed entirely to friction. To match the energy loss, the side-walls and bottom friction term is adjusted heuristically to mimic the energy decay for $U/C_g = 0$ [see Fig. 4(b)].

The presence of a current compresses the waves, forcing the significant wave height to increase soon after entering into the zone of an adverse velocity gradient. This results in a rapid increase of wave steepness and enhancement of nonlinear properties. The rapid change of H_s is well captured by the model for moderate currents ($U/C_g > -0.19$), but it is overestimated for stronger current flows [slightly for $U/C_g = -0.29$ and more substantially for $U/C_g > -0.38$; see Fig. 4(b)]. Subsequently,

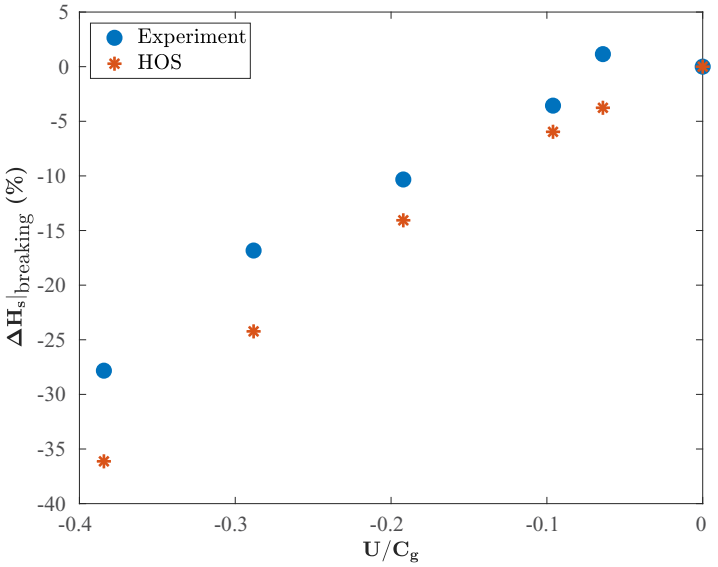

FIG. 5. Energy loss due to wave breaking.

the significant wave height drops as the wave field further develops along the flume. Figure 5 shows that breaking dissipation—defined as the total energy loss throughout the flume minus the energy loss due to friction in the absence of current—remains negligible for $U/Cg > -0.1$, while it contributes significantly to energy loss for $U/Cg < -0.1$. Breaking becomes the dominant source of dissipation for $U/C_g = -0.38$. Although the evolution of H_s for $U/C_g = -0.38$ is reproduced qualitatively well by the model, the latter notably overestimates H_s. It should be mentioned, in this respect, that the Euler's model used herein relies on the assumption of a slowly varying current in the horizontal direction, which may not exactly replicate the experimental conditions. Furthermore, the wave breaking dissipation term was not specifically developed to simulate the intense breaking events induced by strong wave-current interaction. Therefore, the overestimation of significant wave height is not unexpected.

B. The wave energy spectrum

The significant wave height only shows the overall variance of the spectral density. It is, however, instructive to identify how energy is redistributed or lost across the frequency domain. In this respect, the evolution of the wave energy spectrum both in the flume and the numerical wave tank is presented in Fig. 6, noting that the model shows runs with combined friction and breaking dissipation. The input wave spectrum is included as a benchmark. As expected, the spectral density is not replicated exactly in the flume, with the peak being slightly less energetic and the upper tail being slightly more energetic than the input and model spectrum (see top-left panel in Fig. 6). The increase of energy due to the interaction with the current is evident and primarily concentrated around the spectral peak. Energy loss due to friction with no or low current speed and a combination of friction and wave breaking with strong current is also apparent at the peak and especially in the upper tail of the spectrum. Overall, there is a remarkable agreement between the numerical simulations and experimental results. Nevertheless, notable differences are observed for $U/C_g = -0.38$, which denotes model limitations to accurately capture wave breaking dissipation in the presence of strong current gradients (cf. Fig. 5).

There is evidence of a downshift of the spectral peak during propagation (see the evolution of the peak frequency f_p as a function of the nondimensional distance from the wave maker in Fig. 7).

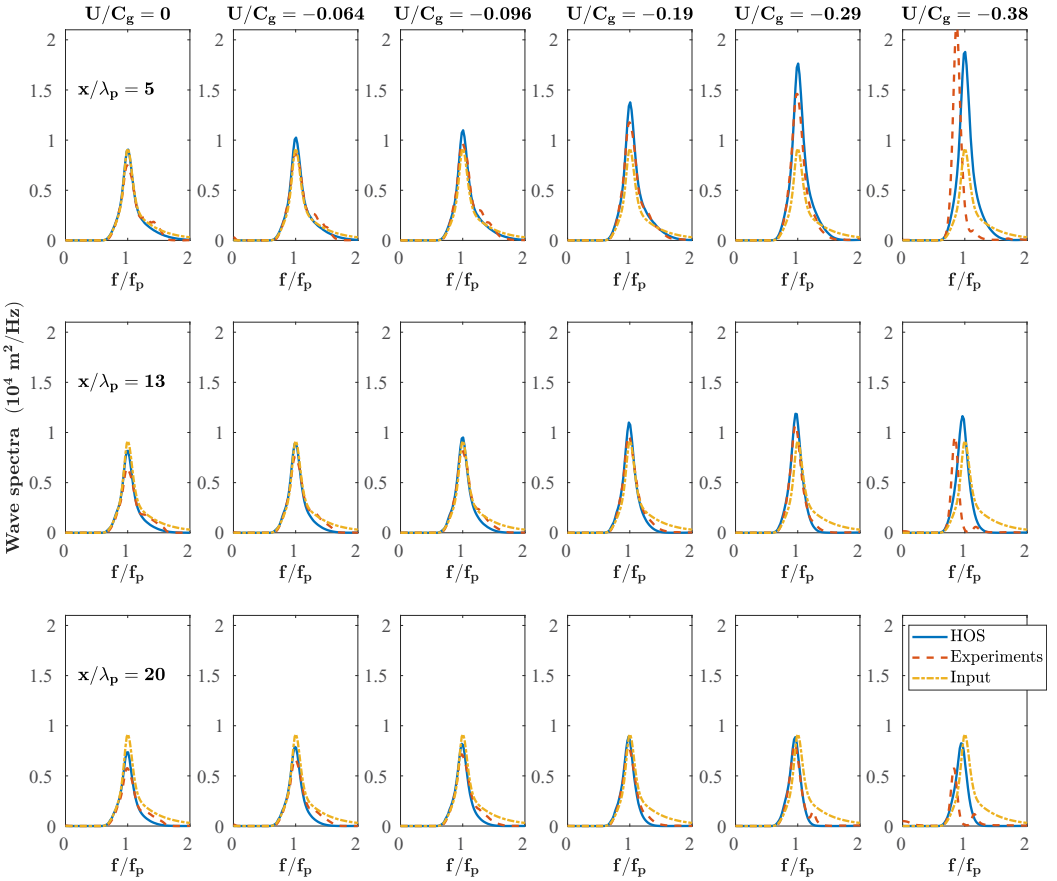

FIG. 6. Evolution of experimental (dashed red line) and numerical (solid blue line) wave spectrum at different distances from the wave maker and different current velocities; the input wave spectrum (dash-dotted yellow line) is presented as a benchmark.

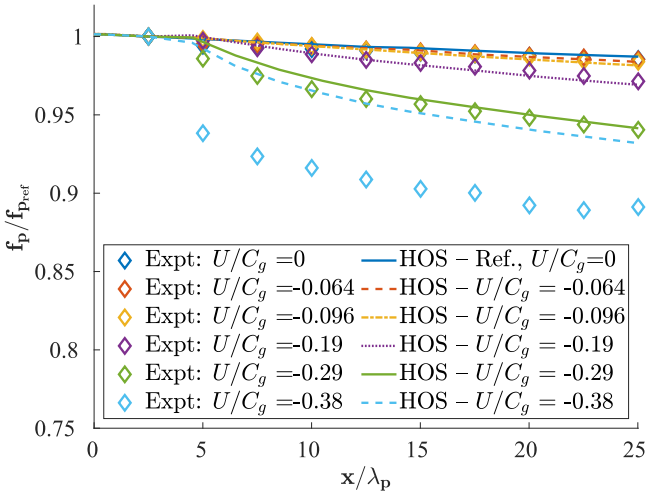

FIG. 7. Evolution of the peak frequency as a function of the distance from the wave maker. Comparison between experiments and numerical simulations.

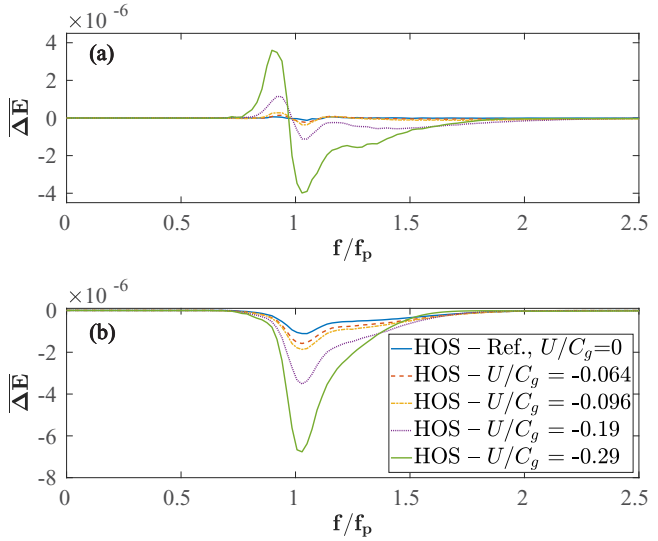

FIG. 8. Average wave energy transfer from numerical simulations: (a) without and (b) with friction and breaking dissipation terms.

The feature develops progressively within 10–20 wavelengths from the wave maker. For no or low current ($U/C_g \geqslant -0.1$), the downshift is almost negligible, while it becomes substantial as current speed increases ($U/C_g < -0.1$). The model captures the feature well for all configurations with $U/Cg \geqslant -0.29$, but it completely diverges from experimental observations for $U/Cg = -0.38$.

To understand the nature of this downshift, the energy transfer and loss, ΔE, across the frequency domain is presented in Fig. 8. The variable is estimated from numerical simulations running without [Fig. 8(a)] and with [Fig. 8(b)] the friction and breaking terms to separate the contribution of nonlinear interactions from the overall dynamics. The term ΔE is calculated as follows:

$$\Delta E = \frac{E_{x_2}(f) - E_{x_1}(f)}{x_2 - x_1}, \tag{4}$$

where $E_{x_i}(f)$ is the wave energy spectrum at a specific location x_i. Note that only configurations with $U/C_g \geqslant -0.29$ are shown in the figure as the model is unstable for strong currents ($U/C_g = -0.38$), if the dissipation term is turned off. Without loss of generality, an average variable is computed along the flume ($\overline{\Delta E}$). The model runs excluding friction and breaking dissipation terms describe the evolution driven by nonlinear interactions. In the absence of current, the weakly nonlinear nature of the initial condition inhibits these interactions and results in a negligible energy redistribution across modes. The opposing current, on the other hand, excites nonlinear properties (wave steepness increases) and consequently triggers a significant energy transfer from high to low frequencies, which contributes to spectral downshift (cf. [11,50,69]). Friction and breaking terms induce an additional and prominent energy loss for modes at approximately $f > 0.9 f_p$ [Fig. 8(b)]. This further contributes to removing energy near the peak and at high frequencies, emphasizing the spectral downshift. The combined contribution of nonlinear interaction and dissipation on the downshift reported herein is consistent with the one reported for wind-generated waves in [70].

C. Wave steepness

As the wave field propagates along the flume, laboratory constraints and interaction with an opposing current alter the properties of the initial wave energy spectrum. The decay of significant wave height and the concurrent spectral downshift produce an evident reduction of the wave

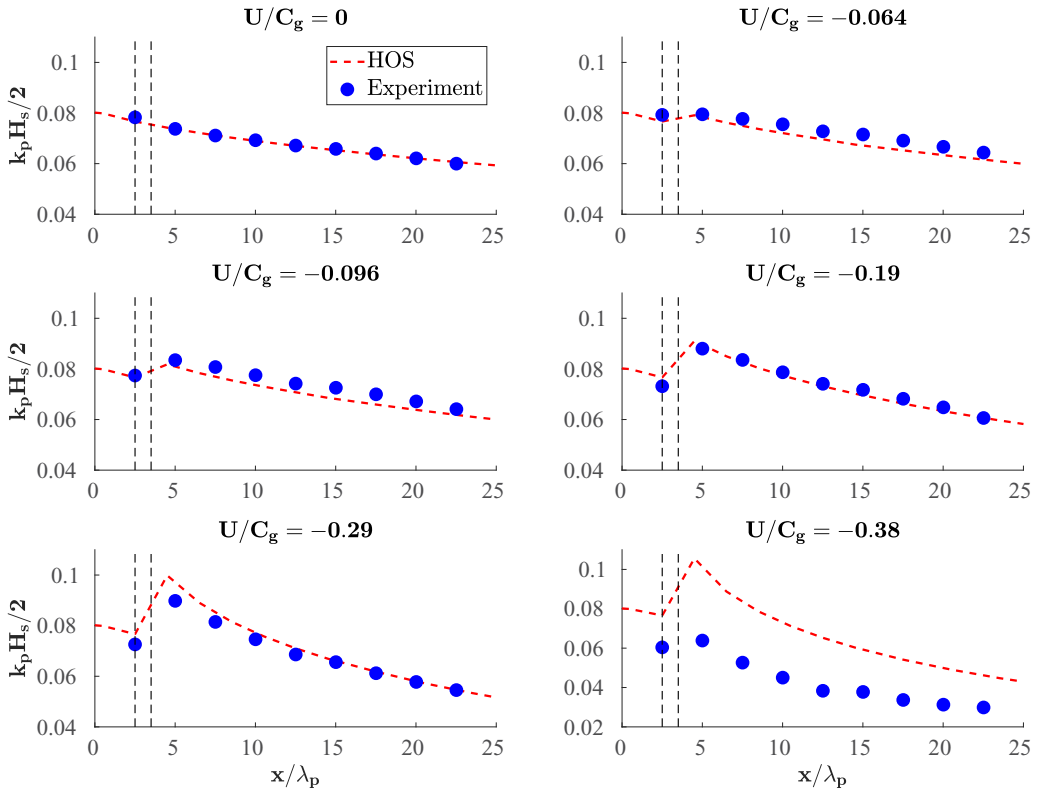

FIG. 9. Evolution of local steepness, $k_pH_s/2$, during wave propagation. Comparison between experiments and numerical simulations.

steepness, which counterbalance the effect of the current gradient (i.e., the initial enhancement of nonlinearity). Figure 9 presents the evolution of the steepness, $k_pH_s/2$, for all current speeds. There is a remarkable agreement between the experiments and numerical simulations for all configurations except $U/Cg = -0.38$. For strong current speeds, the substantial downshift is underpredicted by the model, resulting in a concurrent overprediction of steepness.

V. WAVE STATISTICS

A. Skewness of surface elevation

The skewness of the surface elevation, namely, the third-order moment of its probability density function (PDF), is an indicator of the vertical asymmetry of the wave profile. For a Gaussian random process, the wave profile is symmetric and the skewness is zero. If second-order effects are active, wave crests sharpen and troughs flatten, inducing a positive skewness to the PDF and a consequent weak departure from Gaussian statistics [20]. Figure 10 presents the evolution of the wave skewness, both experimental and numerical, for different current speeds.

The small steepness of the input wave field ($k_pH_s/2 = 0.08$) allows a weak second-order effect to develop. Without background current, the skewness remain small (lower than 0.1) throughout the flume. As the steepness reduces due to frictions, the skewness shows a consistent decay as well. The presence of a current excites second-order effects by enhancing the steepness. As a consequence, the skewness increases with current speed and significantly high values are reported starting from $U/C_g < -0.1$. As for the configuration without current, that skewness gradually decays as a result of energy loss and spectral downshifting. The intensive breaking occurring for very strong currents

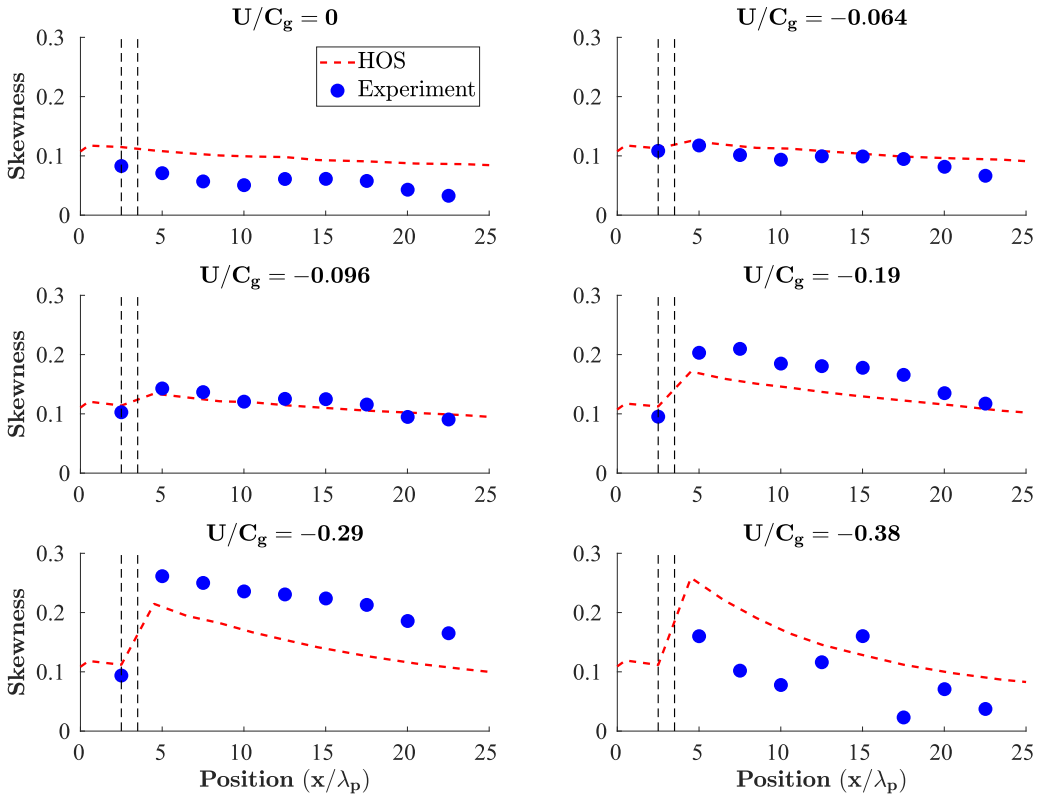

FIG. 10. Spatial evolution of the skewness along the wave flume for different current velocities. Comparison between experiments and numerical simulations.

($U/C_g = -0.38$) limits the height of the wave crests, restraining the vertical asymmetry of the wave field with a concurrent drop of skewness. Note also that there is a more erratic behavior along the flume, substantiating the complexity of the wave field.

The model runs replicate the evolution of second-order effects correctly, but more qualitatively than quantitatively. Without current, the model slightly overestimates the experiments due to the different initial conditions generated in the physical and the numerical wave tanks (see Fig. 6). The simulated skewness is consistent with experiments for slow currents, $U/C_g = -0.06$ and -0.10, while it misses the full extent of the vertical asymmetry of the wave profile and thus underestimates experimental observations for moderate current speeds, $U/C_g = -0.19$ and -0.29. For strong currents $U/C_g = -0.34$, the model overpredicts the skewness as a result of the inaccuracy in the capturing of breaking dissipation.

B. Kurtosis of surface elevation

The fourth-order moment of the probability density function of the surface elevation, i.e., the kurtosis, is a classical indicator of nonlinear properties and a measure of the occurrence of extreme (rogue) waves in a record [26]. For Gaussian (linear) processes, the kurtosis is equal to 3, while it is greater than 3 for non-Gaussian sea states. For water waves, it is reasonable to expect the kurtosis to be about 3.2 for weakly non-Gaussian conditions and between 3.2 and 4 for strongly non-Gaussian conditions [26,27]. The evolution of kurtosis from experimental observations and numerical simulations is shown in Fig. 11 as a function of the distance from the wave maker and for different current speeds.

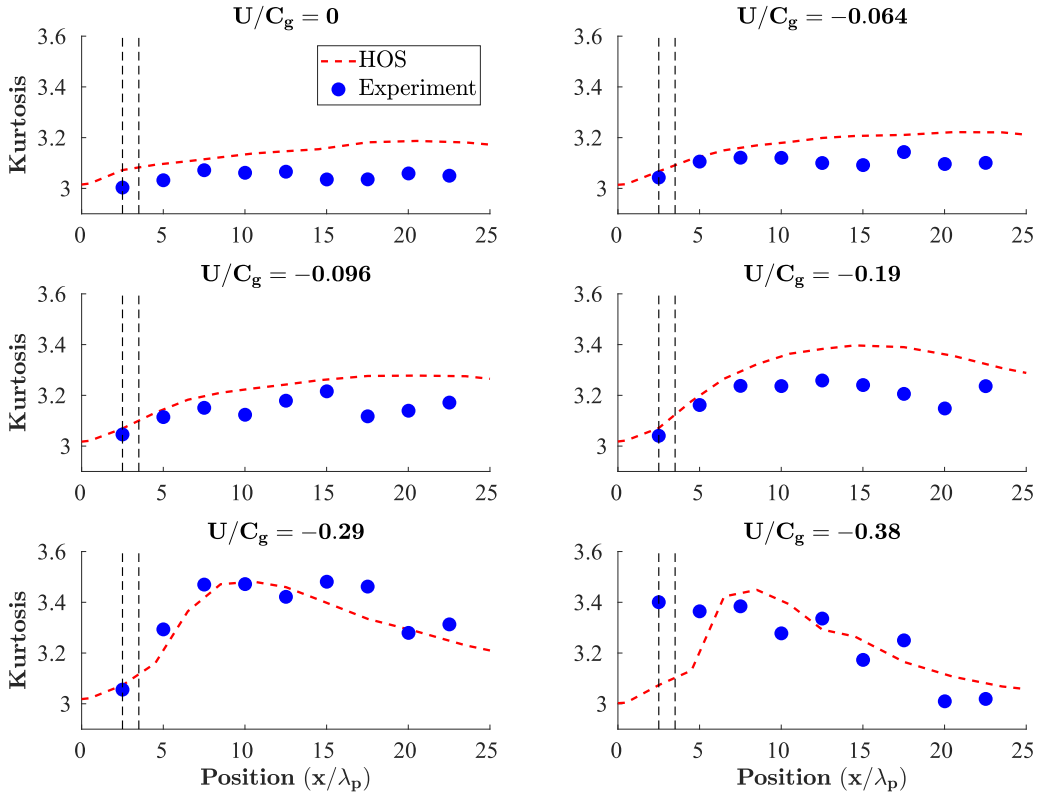

FIG. 11. Spatial evolution of the kurtosis along the wave flume for different current velocities. Comparison between experiments and numerical simulations.

Without a background current, the kurtosis only weakly increases during the first 10 wavelengths, after which it stabilizes around the value of 3.1. This weak departure from the Gaussian distribution is controlled by bound waves generated by second-order interaction [38,71]. The numerical simulations capture the weak evolution of kurtosis, although the model predicts slightly higher values with kurtosis, increasing up to a maximum of about 3.18 after about 20 wavelengths. Note that a small overprediction is somewhat expected for unidirectional waves field as a result of more intense high-order nonlinearity in the numerical simulations [28,58].

The interaction with an opposing current forces the kurtosis to undergo a more substantial dynamics, with the maximum value consequently enhanced (see maximum kurtosis as a function of current speed in Fig. 12). For $U/C_g > -0.19$, the kurtosis remains constant after reaching its maximum, while it drops for $U/C_g \leqslant -0.19$ as a consequence of wave breaking, which puts a limit to the wave height and thus produces a negative feedback on the kurtosis. For strong currents ($U/C_g \leqslant -0.29$), kurtosis is reported to be as high as 3.5, which is an exceptional value for water waves and is normally observed in the laboratory for more nonlinear initial conditions [26–28,58,72,73]. Overall, numerical simulations capture the evolution along the flume well (Fig. 11), noting that the smoother trends are due to the large amount of data from the simulations and the more controlled numerical environment, which avoids reflections and inhomogeneity of the current field for example. It is worth mentioning that the decay of the kurtosis forced by breaking for $U/C_g = -0.29$ and -0.39 is also relatively well captured by the model, although breaking is underestimated by the dissipation (see Fig. 5). Despite a small and consistent overestimation across all configurations, the model replicates the maximum values quantitatively well (see Fig. 12). As the

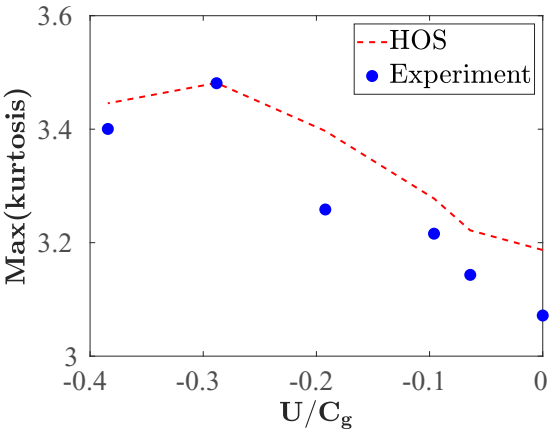

FIG. 12. Maximum of kurtosis in the tank for different current velocities. Comparison between experiments and numerical simulations.

model only replicates third-order nonlinear interactions, the results corroborate that modulational instability activates in the presence of a background current and leads to the formation of a large number of rogue waves in otherwise stable sea states.

C. Exceedance probability of wave height

In the context of rogue waves, it is instructive to present deviations from Gaussian statistics in terms of the exceedance probability of the wave height, $P(H)$. Figure 13 presents the wave height distributions coinciding with the maximum kurtosis for all current speeds; both the experimental and numerical results are reported. As a baseline, the exceedance probability for a linear wave field, computed by turning off the nonlinear terms in the HOS model, is included in the figure. Note that the linear wave height distribution differs from a standard Rayleigh distribution because the wave fields do not satisfy the narrowbanded approximation.

Despite its small steepness, the wave height distribution associated to the input wave field exhibits a weak, yet notable deviation from the linear baseline in the absence of current. The model prediction replicates experimental results well. The presence of current, on the other hand, induces a more substantial deviation from the linear benchmark, which clearly underpredicts the occurrence of waves with nondimensional height, $H/H_s > 1.5$. In terms of rogue waves, which are defined as $H/H_s > 2$, the probability of occurrence increases by almost one order of magnitude due to wave-current interaction: from 3×10^{-4} for $U/C_g = 0$ to 1.2×10^{-3} for $U/C_g = -0.29$. For the strongest current $U/C_g = -0.38$, breaking limits wave height, hampering deviations from the linear prediction.

The HOS model replicates the empirical wave height distribution remarkably well for $U/C_g \leqslant -0.29$. For more intense current speed ($U/C_g = -0.38$), the underestimation of breaking dissipation leads to an overestimation of wave height, which results in a still substantial deviation from the linear prediction compared with the experimental observations.

VI. CONCLUSIONS

The influence of an opposing current on wave dynamics and the emergence of extreme (rogue) waves was assessed with the aid of experimental observations in a wave flume, where wave propagation is confined to unidirectional conditions, and numerical simulations with a current-modified version of the Euler equations solved with a higher-order spectral method. Dissipation terms to account for wall friction and wave breaking were included to model the energy loss along the

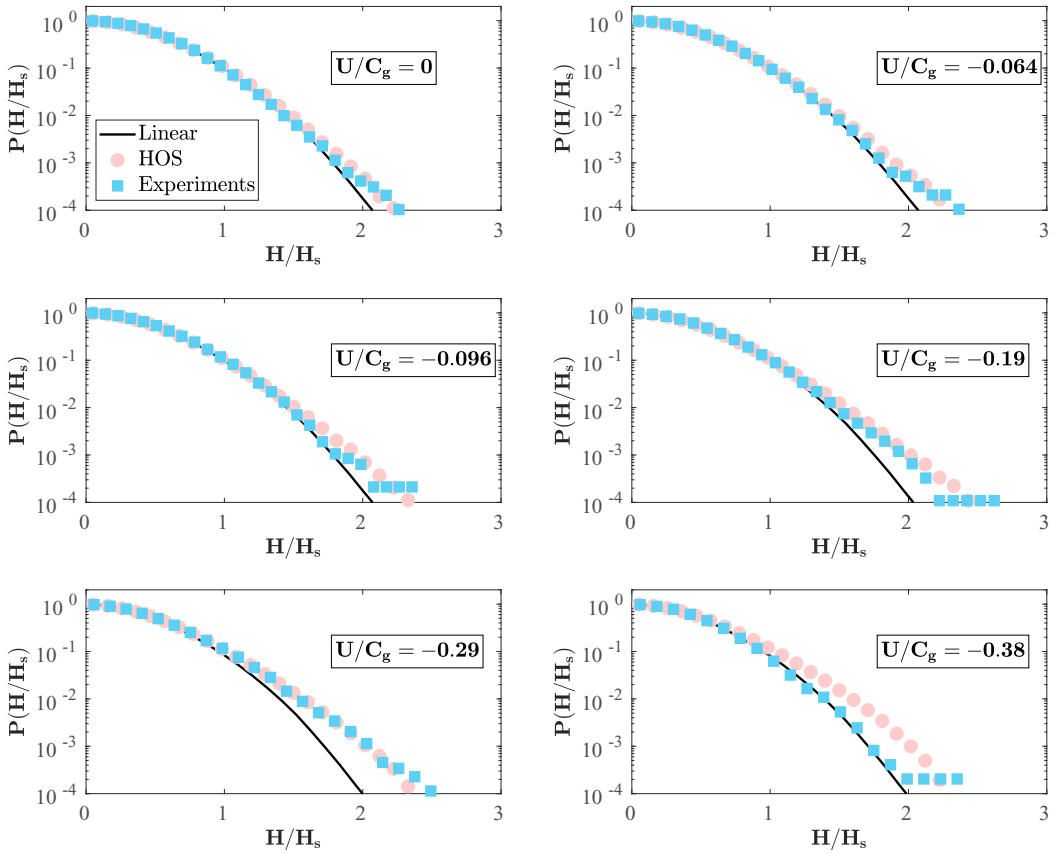

FIG. 13. Plots of the exceedance probability of wave height at the location of maximum kurtosis for different current velocities. Comparison between experiments and numerical simulations.

flume. The initial conditions were imposed at the wave maker and model boundaries in the form of a JONSWAP wave spectrum configured with spectral peak period of 0.8 s, significant wave height of 0.025 m (i.e., wave steepness $k_p H_s/2 = 0.08$), and peak enhancement factor $\gamma = 3$. The initial conditions ensure a weak level of nonlinearity to hamper the development of modulational instability. The evolution of the wave field was monitored at specified distances from the wave maker (and model boundaries) without and with background current fields with velocity U normalized by the wave group velocity C_g up to to -0.38.

In response to the current field, the sea state exhibited a sudden increase of the significant wave height, followed by a contraction of the wavelength due to a Doppler effect. As a result, the steepness increased, strengthening the nonlinear properties of the wave field. As propagation continued, the wave field showed an evident spectral downshift and a significant energy loss, ranging from about 20% in the absence of current to about 60% with the strongest current speed, $U/C_g = -0.38$. Analysis of wave statistics evidenced an intensification of non-Gaussian properties. These included a positive skewness, indicating a more vertically asymmetric profile with higher crests and flattened troughs, and high kurtosis (up to 3.5), substantiating the emergence of a significantly large number of extreme waves. The latter was further emphasized by heavy tails in the exceedance probability distribution of wave heights.

The numerical model captures well, both qualitatively and quantitatively, the evolution of basic features of the wave field—such as wave height, wave steepness, and spectral shape—and

concurrent statistical properties—such as skewness, kurtosis, and wave height distribution. Furthermore, simulations reveal insights into the nonlinear wave dynamics over an opposing current; specifically: (i) an opposing current enhances nonlinearity and forces an energy transfer from high- to low-frequency modes, which control the spectral downshift (note that the dominant wave component becomes less prone to the effect of the current by downshifting towards lower frequencies); (ii) rogue waves can emerge as a result of quasiresonant nonlinear interactions in otherwise stable random wave fields; and (iii) wave breaking dissipation becomes relevant for current speed with $U/C_g < -0.19$, contributing up to 40% of the energy loss (note that breaking further accelerates the downshift by selectively removing energy at high-frequency modes). It is worth mentioning that the dissipation term implemented in the model was not specifically developed to predict the intense wave breaking for very strong currents ($U/C_g = -0.38$), thus resulting in an overestimation of significant wave height, peak period, and wave steepness for this configuration. Surprisingly, however, the statistical properties have not been notably affected by uncertainties in breaking dissipation.

ACKNOWLEDGMENTS

This research was funded by the Cooperative Research Centres Projects (CRC-P) initiative of the Australian Government (Grant No. CRC-P53991). The authors acknowledge Prof. D. Greaves, Dr. K. Collins, and Dr. M. Hann for granting access to and providing technical support for experimental facilities at the University of Plymouth. A.T. and F.N. acknowledge technical support from the Air-Sea-Ice Lab Project initiative.

[1] L. H. Holthuijsen, *Waves in Oceanic and Coastal Waters* (Cambridge University Press, Cambridge, 2010).

[2] S. Haver and O. J. Andersen, Freak waves: Rare realizations of a typical population or typical realizations of a rare population? in *The Tenth International Offshore and Polar Engineering Conference*, edited by J. S. Chung, R. Frederking, H. Saeki, and W. Koterayama (International Society of Offshore and Polar Engineers, Cupertino, 2000).

[3] I. I. Didenkulova, A. V. Slunyaev, E. N. Pelinovsky, and C. Kharif, Freak waves in 2005, Nat. Hazards Earth Syst. Sci **6**, 1007 (2006).

[4] A. Benetazzo, F. Barbariol, F. Bergamasco, A. Torsello, S. Carniel, and M. Sclavo, Observation of extreme sea waves in a space-time ensemble, J. Phys. Oceanogr. **45**, 2261 (2015).

[5] A. Karin Magnusson and M. A. Donelan, The Andrea wave characteristics of a measured North Sea rogue wave, J. Offshore Mech. Arct. **135**, 031108 (2013).

[6] C. Kharif and E. Pelinovsky, Physical mechanisms of the rogue wave phenomenon, Eur. J. Mech. B Fluids **22**, 603 (2003).

[7] P. A. E. M. Janssen, Nonlinear four-wave interactions and freak waves, J. Phys. Oceanogr. **33**, 863 (2003).

[8] A. Osborne, *Nonlinear Ocean Waves and the Inverse Scattering Transform* (Academic Press, New York, 2010).

[9] M. Onorato, S. Residori, U. Bortolozzo, A. Montina, and F. T. Arecchi, Rogue waves and their generating mechanisms in different physical contexts, Phys. Rep. **528**, 47 (2013).

[10] M. Onorato, A. R. Osborne, and M. Serio, Modulational Instability in Crossing Sea States: A Possible Mechanism for the Formation of Freak Waves, Phys. Rev. Lett. **96**, 014503 (2006).

[11] M. Onorato, T. Waseda, A. Toffoli, L. Cavaleri, O. Gramstad, P. A. E. M. Janssen, T. Kinoshita, J. Monbaliu, N. Mori, A. R. Osborne, M. Serio, C. T. Stansberg, H. Tamura, and K. Trulsen, Statistical Properties of Directional Ocean Waves: The Role of the Modulational Instability in the Formation of Extreme Events, Phys. Rev. Lett. **102**, 114502 (2009).

[12] A. Chabchoub, N. P. Hoffmann, and N. Akhmediev, Rogue Wave Observation in a Water Wave Tank, Phys. Rev. Lett. **106**, 204502 (2011).

[13] A. Toffoli, T. Waseda, H. Houtani, L. Cavaleri, D. Greaves, and M. Onorato, Rogue waves in opposing currents: An experimental study on deterministic and stochastic wave trains, J. Fluid Mech. **769**, 277 (2015).

[14] A. Toffoli, T. Waseda, H. Houtani, T. Kinoshita, K. Collins, D. Proment, and M. Onorato, Excitation of rogue waves in a variable medium: An experimental study on the interaction of water waves and currents, Phys. Rev. E **87**, 051201(R) (2013).

[15] A. Chabchoub, K. Mozumi, N. Hoffmann, A. V. Babanin, A. Toffoli, J. N. Steer, T. S. van den Bremer, N. Akhmediev, M. Onorato, and T. Waseda, Directional soliton and breather beams, Proc. Natl. Acad. Sci. USA **116**, 9759 (2019).

[16] M. L. McAllister, S. Draycott, T. A. A. Adcock, P. H. Taylor, and T. S. van den Bremer, Laboratory recreation of the Draupner wave and the role of breaking in crossing seas, J. Fluid Mech. **860**, 767 (2019).

[17] G. F. Clauss, Dramas of the sea: Episodic waves and their impact on offshore structures, Appl. Ocean Res. **24**, 147 (2002).

[18] A. Toffoli, J. M. Lefevre, E. Bitner-Gregersen, and J. Monbaliu, Towards the identification of warning criteria: Analysis of a ship accident database, Appl. Ocean Res. **27**, 281 (2005).

[19] L. Cavaleri, L. Bertotti, L. Torrisi, E. Bitner-Gregersen, M. Serio, and M. Onorato, Rogue waves in crossing seas: The Louis Majesty accident, J. Geophys. Res. **117**, C00J10 (2012).

[20] G. Z. Forristall, Wave crest distributions: Observations and second-order theory, J. Phys. Oceanogr. **30**, 1931 (2000).

[21] P. Peterson, T. Soomere, J. Engelbrecht, and E. van Groesen, Soliton interaction as a possible model for extreme waves in shallow water, Nonlinear Proc. Geophys. **10**, 503 (2003).

[22] A. Toffoli, M. Onorato, and J. Monbaliu, Wave statistics in unimodal and bimodal seas from a second-order model, Eur. J. Mech. B Fluids **25**, 649 (2006).

[23] K. Trulsen, J. C. Nieto Borge, O. Gramstad, L. Aouf, and J.-M. Lefèvre, Crossing sea state and rogue wave probability during the Prestige accident, J. Geophys. Res. **120**, 7113 (2015).

[24] F. Fedele, J. Brennan, S. P. De León, J. Dudley, and F. Dias, Real World ocean rogue waves explained without the modulational instability, Sci. Rep. **6**, 27715 (2016).

[25] P. Janssen and P. A. E. M. Janssen, *The Interaction of Ocean Waves and Wind* (Cambridge University Press, Cambridge, 2004).

[26] M. Onorato, L. Cavaleri, S. Fouques, O. Gramstad, P. A. E. M. Janssen, J. Monbaliu, A. R. Osborne, C. Pakozdi, M. Serio, C. T. Stansberg *et al.*, Statistical properties of mechanically generated surface gravity waves: A laboratory experiment in a three-dimensional wave basin, J. Fluid Mech. **627**, 235 (2009).

[27] T. Waseda, T. Kinoshita, and H. Tamura, Evolution of a random directional wave and freak wave occurrence, J. Phys. Oceanogr. **39**, 621 (2009).

[28] A. Toffoli, O. Gramstad, K. Trulsen, J. Monbaliu, E. Bitner-Gregersen, and M. Onorato, Evolution of weakly nonlinear random directional waves: Laboratory experiments and numerical simulations, J. Fluid Mech. **664**, 313 (2010).

[29] A. Toffoli, E. M. Bitner-Gregersen, A. R. Osborne, M. Serio, J. Monbaliu, and M. Onorato, Extreme waves in random crossing seas: Laboratory experiments and numerical simulations, Geophys. Res. Lett. **38**, L06605 (2011).

[30] O. Gramstad, E. Bitner-Gregersen, K. Trulsen, and J. C. Nieto Borge, Modulational instability and rogue waves in crossing sea states, J. Phys. Oceanogr. **48**, 1317 (2018).

[31] N. Mori and T. Yasuda, Effects of high-order nonlinear interactions on unidirectional wave trains, Ocean Eng. **29**, 1233 (2002).

[32] H. Socquet-Juglard, K. Dysthe, K. Trulsen, H. E. Krogstad, and J. Liu, Probability distributions of surface gravity waves during spectral changes, J. Fluid Mech. **542**, 195 (2005).

[33] E. M. Bitner-Gregersen, L. Fernández, J. M. Lefèvre, J. Monbaliu, and A. Toffoli, The North Sea Andrea storm and numerical simulations, Nat. Haz. Earth Syst. Sci. **14**, 1407 (2014).

[34] W. Fujimoto, T. Waseda, and A. Webb, Impact of the four-wave quasi-resonance on freak wave shapes in the ocean, Ocean Dyn. **69**, 101 (2019).

[35] A. V. Babanin, T. Waseda, T. Kinoshita, and A. Toffoli, Wave breaking in directional fields, J. Phys. Oceanogr. **41**, 145 (2011).

[36] E. Fadaeiazar, A. Alberello, M. Onorato, J. Leontini, F. Frascoli, T. Waseda, and A. Toffoli, Wave turbulence and intermittency in directional wave fields, Wave Motion **83**, 94 (2018).
[37] E. Fadaeiazar, J. Leontini, M. Onorato, T. Waseda, A. Alberello, and A. Toffoli, Fourier amplitude distribution and intermittency in mechanically generated surface gravity waves, Phys. Rev. E **102**, 013106 (2020).
[38] S. Y. Annenkov and V. I. Shrira, Evolution of kurtosis for wind waves, Geophys. Res. Lett. **36**, L13603 (2009).
[39] C. Viotti and F. Dias, Extreme waves induced by strong depth transitions: Fully nonlinear results, Phys. Fluids **26**, 051705 (2014).
[40] K. Trulsen, A. Raustøl, S. Jorde, and L. B. Rye, Extreme wave statistics of long-crested irregular waves over a shoal, J. Fluid Mech. **882**, R2 (2020).
[41] G. Ducrozet and M. Gouin, Influence of varying bathymetry in rogue wave occurrence within unidirectional and directional sea-states, J. Ocean Eng. Marine Energy **3**, 309 (2017).
[42] J. R. Stocker and D. H. Peregrine, The current-modified nonlinear Schrödinger equation, J. Fluid Mech. **399**, 335 (1999).
[43] A. Toffoli, L. Cavaleri, A. V. Babanin, M. Benoit, E. M. Bitner-Gregersen, J. Monbaliu, M. Onorato, A. R. Osborne, and C. T. Stansberg, Occurrence of extreme waves in three-dimensional mechanically generated wave fields propagating over an oblique current, Nat. Haz. Earth Syst. Sci. **11**, 895 (2011).
[44] I. V. Lavrenov, The wave energy concentration at the Agulhas current off South Africa, Nat. Haz. **17**, 117 (1998).
[45] B. S. White and B. Fornberg, On the chance of freak waves at sea, J. Fluid Mech. **355**, 113 (1998).
[46] E. J. Heller, L. Kaplan, and A. Dahlen, Refraction of a Gaussian seaway, J. Geophys. Res.: Oceans **113**, C09023 (2008).
[47] A. Chawla and J. T. Kirby, Monochromatic and random wave breaking at blocking points, J. Geophys. Res.: Oceans **107**, 4 (2002).
[48] Y. Ma, G. Dong, M. Perlin, X. Ma, G. Wang, and J. Xu, Laboratory observations of wave evolution, modulation and blocking due to spatially varying opposing currents, J. Fluid Mech. **661**, 108 (2010).
[49] A. Toffoli, L. Fernandez, J. Monbaliu, M. Benoit, E. Gagnaire-Renou, J. M. Lefevre, L. Cavaleri, D. Proment, C. Pakozdi, C. T. Stansberg *et al.*, Experimental evidence of the modulation of a plane wave to oblique perturbations and generation of rogue waves in finite water depth, Phys. Fluids **25**, 091701 (2013).
[50] T. Waseda, T. Kinoshita, L. Cavaleri, and A. Toffoli, Third-order resonant wave interactions under the influence of background current fields, J. Fluid Mech. **784**, 51 (2015).
[51] H. Rapizo, T. Waseda, A. V. Babanin, and A. Toffoli, Laboratory experiments on the effects of a variable current field on the spectral geometry of water waves, J. Phys. Oceanogr. **46**, 2695 (2016).
[52] M. Onorato, D. Proment, and A. Toffoli, Triggering Rogue Waves in Opposing Currents, Phys. Rev. Lett. **107**, 184502 (2011).
[53] G. J. Komen, L. Cavaleri, M. Donelan, K. Hasselmann, S. Hasselmann, and P. A. E. M. Janssen, *Dynamics and Modelling of Ocean Waves* (Cambridge University Press, Cambridge, 1996), p. 554.
[54] G. Ducrozet, F. Bonnefoy, D. Le Touzé, and P. Ferrant, HOS-OCEAN: Open-source solver for nonlinear waves in open ocean based on high-order spectral method, Comput. Phys. Commun. **203**, 245 (2016).
[55] M. Tanaka, Verification of Hasselmann's energy transfer among surface gravity waves by direct numerical simulations of primitive equations, J. Fluid Mech. **444**, 199 (2001).
[56] A. Toffoli, M. Onorato, E. M. Bitner-Gregersen, and J. Monbaliu, Development of a bimodal structure in ocean wave spectra, J. Geophys. Res.: Oceans **115**, C03006 (2010).
[57] G. Ducrozet, F. Bonnefoy, D. Le Touzé, and P. Ferrant, 3D HOS simulations of extreme waves in open seas, Nat. Haz. Earth Syst. Sci. **7**, 109 (2007).
[58] W. Xiao, Y. Liu, G. Wu, and D. K. P. Yue, Rogue wave occurrence and dynamics by direct simulations of nonlinear wave-field evolution, J. Fluid Mech. **720**, 357 (2013).
[59] G. Wu, Direct simulation and deterministic prediction of large-scale nonlinear ocean wave-field, Ph.D. thesis, Massachusetts Institute of Technology, 2004.

[60] C. C. Mei, M. Stiassnie, and D. K.-P. Yue, *Theory and Applications of Ocean Surface Waves: Nonlinear Aspects* (World Scientific, Singapore, 2005), Vol. 23.
[61] M. Gouin, G. Ducrozet, and P. Ferrant, Development and validation of a non-linear spectral model for water waves over variable depth, Eur. J. Mech. B Fluids **57**, 115 (2016).
[62] M. Gouin, G. Ducrozet, and P. Ferrant, Propagation of 3D nonlinear waves over an elliptical mound with a high-order spectral method, Eur. J. Mech. B Fluids **63**, 9 (2017).
[63] B. J. West, K. A. Brueckner, R. S. Janda, D. M. Milder, and R. L. Milton, A new numerical method for surface hydrodynamics, J. Geophys. Res.: Oceans **92**, 11803 (1987).
[64] F. Bonnefoy, G. Ducrozet, D. Le Touzé, and P. Ferrant, Time domain simulation of nonlinear water waves using spectral methods, in *Advances in Numerical Simulation of Nonlinear Water Waves* (World Scientific, Singapore, 2010), pp. 129–164.
[65] D. M. Henderson and R. C. Lee, Laboratory generation and propagation of ripples, Phys. Fluids **29**, 619 (1986).
[66] B. R. Seiffert, G. Ducrozet, and F. Bonnefoy, Simulation of breaking waves using the high-order spectral method with laboratory experiments: Wave-breaking onset, Ocean Model. **119**, 94 (2017).
[67] B. R. Seiffert and G. Ducrozet, Simulation of breaking waves using the high-order spectral method with laboratory experiments: Wave-breaking energy dissipation, Ocean Dyn. **68**, 65 (2018).
[68] A. Toffoli, A. V. Babanin, M. Onorato, and T. Waseda, Maximum steepness of oceanic waves: Field and laboratory experiments, Geophys. Res. Lett. **37**, L05603 (2010).
[69] T. Waseda, T. Kinoshita, and H. Tamura, Interplay of resonant and quasi-resonant interaction of the directional ocean waves, J. Phys. Oceanogr. **39**, 2351 (2009).
[70] M. P. Tulin and T. Waseda, Laboratory observations of wave group evolution, including breaking effects, J. Fluid Mech. **378**, 197 (1999).
[71] M. A. Tayfun, Narrow-band nonlinear sea waves, J. Geophys. Res. **85**, 1548 (1980).
[72] M. Onorato, A. R. Osborne, M. Serio, L. Cavaleri, C. Brandini, and C. T. Stansberg, Extreme waves, modulational instability and second order theory: Wave flume experiments on irregular waves, Eur. J. Mech. B Fluids **25**, 586 (2006).
[73] L. Shemer and A. Sergeeva, An experimental study of spatial evolution of statistical parameters in a unidirectional narrow-banded random wavefield, J. Geophys. Res.: Oceans **114**, C01015 (2009).